Multi-resolution HWENO schemes for hyperbolic conservation laws

Jiayin Li[1], Chi-Wang Shu[2] and Jianxian Qiu[3]

Abstract

In this paper, a new type of high-order finite volume and finite difference multi-resolution Hermite weighted essentially non-oscillatory (HWENO) schemes are designed for solving hyperbolic conservation laws on structured meshes. Here we only use the information defined on a hierarchy of nested central spatial stencils but do not introduce any equivalent multi-resolution representation, the terminology of multi-resolution HWENO follows that of the multi-resolution WENO schemes [J. Comput. Phys., 375 (2018), 659-683]. The main idea of our spatial reconstruction is derived from the original HWENO schemes [J. Comput. Phys., 193 (2004), 115-135], in which both the function and its first-order derivative values are evolved in time and used in the reconstruction. Our HWENO schemes use the same large stencils as the classical HWENO schemes which are narrower than the stencils of the classical WENO schemes for the same order of accuracy. Only the function values need to be reconstructed by our HWENO schemes, the first-order derivative values are obtained from the high-order linear polynomials directly. Furthermore, the linear weights of such HWENO schemes can be any positive numbers as long as their sum equals one, and there is no need to do any modification or positivity-preserving flux limiting in our numerical experiments. Extensive benchmark examples are performed to illustrate the robustness and good performance of such finite volume and finite difference HWENO schemes.

Key Words: Multi-resolution scheme; HWENO scheme; Hyperbolic conservation laws; Finite volume method; Finite difference method.

AMS(MOS) subject classification: 65M60, 35L65

[1]School of Mathematical Sciences, Xiamen University, Xiamen, Fujian 361005, P.R. China. E-mail: jiayin@stu.xmu.edu.cn.

[2]Division of Applied Mathematics, Brown University, Providence, RI 02912. E-mail: Chi-Wang_Shu@brown.edu. Research is partly supported by AFOSR grant FA9550-20-1-0055 and NSF grant DMS-2010107.

[3]School of Mathematical Sciences and Fujian Provincial Key Laboratory of Mathematical Modeling and High-Performance Scientific Computing, Xiamen University, Xiamen, Fujian 361005, P.R. China. E-mail: jxqiu@xmu.edu.cn. Research is partly supported by Science Challenge Project No. TZ2016002 and NSFC grant 12071392.

1 Introduction

In this paper, a new type of high-order finite volume and finite difference multi-resolution Hermite weighted essentially non-oscillatory (HWENO) schemes are designed for solving the hyperbolic conservation laws

$$\begin{cases} u_t + \nabla \cdot f(u) = 0, \\ u(x_1, ..., x_n, 0) = u_0(x_1, ..., x_n). \end{cases} \tag{1.1}$$

Hyperbolic conservation laws can be used to model a wide variety of phenomena involving wave motion and the advection transport of substances. The problem is that it is quite difficult to solve these problems on both mathematical and numerical aspects, since discontinuities may appear in the solutions of these nonlinear equations even though the initial conditions are smooth enough. This is also why designing high-order and efficient approaches to solve these problems is of great importance and why more and more researchers are interested in it. Under this background, many numerical methods have emerged. Here, we would like to mention essentially non-oscillatory (ENO) [9, 22, 23], weighted essentially non-oscillatory (WENO) schemes [12, 17] and Hermite weighted essentially non-oscillatory (HWENO) schemes [19, 20, 25, 27, 28], which work quite well to solve these problems with strong shocks or contact discontinuities.

In 1987, Harten et al. proposed a series of finite volume ENO schemes for one-dimensional problems in [9] based on the total variation diminishing (TVD) schemes in [8]. In 1988 and 1989, Shu and Osher presented a class of finite difference ENO schemes in [22, 23], which are more efficient for multi-dimensional problems. The main idea of these ENO schemes is to choose the locally smoothest stencil automatically among all the central and biased spatial stencils to keep high-order accuracy in smooth regions and to avoid oscillations near discontinuities. In 1994, Liu et al. proposed the first WENO schemes in [17], which use a nonlinear convex combination of all the candidate stencils instead of the locally smoothest stencil to improve the order of accuracy in smooth regions without destroying the non-oscillatory behavior near discontinuities. In 1996, Jiang and Shu improved the WENO

schemes to fifth order and designed general smoothness indicators and nonlinear weights in [12]. Thereafter, compact central WENO (CWENO) schemes in [7, 13, 14], monotonicity preserving WENO schemes in [3], optimized WENO schemes in [24], hybrid compact WENO schemes in [18], multi-domain hybrid spectral-WENO in [6], WENO-Z in [4], robust WENO schemes in [11], multi-resolution WENO schemes in [29, 30], an efficient class of WENO schemes with adaptive order for structured and unstructured meshes in [1, 2] were developed. ENO and WENO schemes have the following advantages: uniform high-order accuracy in smooth regions including smooth extrema and non-oscillatory behavior near discontinuities.

In 2004, based on the idea of WENO schemes, Qiu and Shu proposed a class of HWENO schemes on a finite volume formulation for one-dimensional problems in [19] and then in 2005, they extended these HWENO schemes to two-dimensional problems in [20], where two different stencils were used to reconstruct the function and its first-order derivative values. However, the first HWENO schemes in [19, 20] failed in simulating several severe problems stably, including the double Mach and the forward step problems. This is because the solutions of these nonlinear hyperbolic conservation laws contain strong discontinuities, and their first-order derivative values may be very large near these discontinuities. If such large first-order derivative values are used straightforwardly, stability issues may arise. Thereafter, in 2008, Zhu and Qiu proposed a new procedure to reconstruct the first-order derivative values to solve this problem in [28], while in 2015 and 2016, Liu and Qiu also solved this problem by applying an additional positivity-preserving procedure in [15, 16]. Then in 2020, Zhao et al. took the idea of the limiter for the discontinuous Galerkin (DG) method in [5] to modify the first-order moments near the discontinuities in [26], in which high-order linear approximation was used in smooth regions, while the first-order moments on the troubled-cells were modified with the HWENO reconstruction. Later, Zhao and Qiu improved the above hybrid HWENO scheme by using a nonlinear convex combination of a high-degree polynomial with several lower-degree polynomials, with the linear weights being any positive numbers as long as their sum equals one, in [27]. The main difference of HWENO schemes

from WENO schemes is that both the function and its first-order derivative values are evolved in time and used in the reconstruction, not like the WENO schemes in which only the function values are evolved and used. This also allows the HWENO schemes to obtain the same order of accuracy as the WENO schemes with narrower stencils.

In this paper, following the idea of multi-resolution WENO schemes proposed by Zhu and Shu in [29, 30], we present a new type of multi-resolution HWENO schemes. Comparing with the multi-resolution WENO schemes in [29, 30], there are several features in common: the first is that we also use a hierarchy of central spatial stencils; the second is that the linear weights can also be any positive numbers as long as their sum equals one. There are also some differences: the first is that not only the function values but also its first-order derivative values are evolved and used, thus we can obtain higher order accuracy with the same number of cells in comparison with the multi-resolution WENO schemes; the second is that only the function values are reconstructed by the multi-resolution HWENO schemes, its first-order derivative values are reconstructed by the high-order linear approximation, which is also different from the previous HWENO schemes. Comparing with the HWENO schemes proposed before, our HWENO schemes do have a few other advantages: the first is that there is no need to modify the first-order derivative values of the target cell before the reconstruction or apply any positivity-preserving flux limiter, to run the numerical experiments with strong shocks stably, at least for the examples we have calculated; the second is that the CFL number can be taken to be 0.6 for both the one and two dimensional cases, while the CFL number is taken to be 0.2 in [15, 16]. In the meantime, our HWENO schemes could also obtain the optimal high-order of accuracy in smooth regions and simultaneously keep sharp transitions with non-oscillatory performance near discontinuities.

The organization of this paper is as follows: In Section 2, at first, we will describe the reconstruction procedure of finite volume multi-resolution HWENO schemes for solving the conservation laws in one and two dimensions in detail. Then, we will describe the reconstruction procedure of finite difference multi-resolution HWENO schemes for solving

the conservation laws in one and two dimensions in detail. In Section 3, we will propose a number of numerical examples to illustrate the accuracy and resolution of these HWENO schemes. Concluding remarks are given in Section 4.

2 Multi-resolution HWENO schemes

In this section, we introduce the finite volume and finite difference multi-resolution HWENO schemes for solving the hyperbolic conservation laws in one and two dimensions in detail.

2.1 Finite volume multi-resolution HWENO schemes

2.1.1 One dimensional case

We first consider the hyperbolic conservation laws (1.1) in one dimension

$$\begin{cases} u_t + f(u)_x = 0, \\ u(x,0) = u_0(x). \end{cases} \tag{2.1}$$

Let $v = u_x$, and then from (2.1) and its spacial derivative, we obtain the following equations

$$\begin{cases} u_t + f(u)_x = 0, \quad u(x,0) = u_0(x), \\ v_t + g(u,v)_x = 0, \quad v(x,0) = v_0(x), \end{cases} \tag{2.2}$$

where $g(u,v) = f'(u)u_x = f'(u)v$. For simplicity, we consider a uniform cell mesh $\{x_{i+1/2}\}$ with the uniform mesh size $h = x_{i+1/2} - x_{i-1/2}$ and denote the cell by $I_i = [x_{i-1/2}, x_{i+1/2}]$ and its center by $x_i = \frac{1}{2}(x_{i-1/2} + x_{i+1/2})$.

We denote the one-dimensional cell averages of u and v as

$$\begin{cases} \overline{u}_i(t) = \frac{1}{h}\int_{I_i} u(x,t)dx, \\ \overline{v}_i(t) = \frac{1}{h}\int_{I_i} v(x,t)dx, \end{cases} \tag{2.3}$$

then integrate (2.2) over the target cell I_i to obtain the integral formulation of the conservation laws

$$\begin{cases} \frac{d\overline{u}_i(t)}{dt} = -\frac{1}{h}\Big(f\big(u(x_{i+1/2},t)\big) - f\big(u(x_{i-1/2},t)\big)\Big), \\ \frac{d\overline{v}_i(t)}{dt} = -\frac{1}{h}\Big(g\big(u(x_{i+1/2},t), v(x_{i+1/2},t)\big) - g\big(u(x_{i-1/2},t), v(x_{i-1/2},t)\big)\Big). \end{cases} \tag{2.4}$$

We approximate (2.4) by the following semi-discrete conservative scheme

$$\begin{cases} \frac{d\overline{u}_i(t)}{dt} = -\frac{1}{h}(\hat{f}_{i+1/2} - \hat{f}_{i-1/2}), \\ \frac{d\overline{v}_i(t)}{dt} = -\frac{1}{h}(\hat{g}_{i+1/2} - \hat{g}_{i-1/2}), \end{cases} \tag{2.5}$$

where the numerical fluxes $\hat{f}_{i+1/2}$ and $\hat{g}_{i+1/2}$ are defined by

$$\begin{cases} \hat{f}_{i+1/2} = \hat{f}(u^-_{i+1/2}, u^+_{i+1/2}), \\ \hat{g}_{i+1/2} = \hat{g}(u^-_{i+1/2}, u^+_{i+1/2}; v^-_{i+1/2}, v^+_{i+1/2}), \end{cases} \tag{2.6}$$

where $u^{\pm}_{i+1/2}$ and $v^{\pm}_{i+1/2}$ are the numerical approximations to the point values of $u(x_{i+1/2}, t)$ and $v(x_{i+1/2}, t)$ respectively from left and right by the HWENO reconstruction procedure. We choose the Lax-Friedrichs fluxes, which are subject to the usual conditions for numerical fluxes, such as Lipschitz continuity and consistency with the physical fluxes

$$\begin{cases} \hat{f}(a, b) = \frac{1}{2}\Big[f\big(a\big) + f\big(b\big) - \alpha\big(b - a\big)\Big], \\ \hat{g}(a, b; c, d) = \frac{1}{2}\Big[g\big(a, c\big) + g\big(b, d\big) - \alpha\big(d - c\big)\Big], \end{cases} \tag{2.7}$$

where $\alpha = \max_u |f'(u)|$ over the whole range of u.

The most important part of the HWENO schemes is the spatial reconstruction of the point values $\{u^{\pm}_{i+1/2}, v^{\pm}_{i+1/2}\}$ from the given cell-average values $\{\overline{u}_i, \overline{v}_i\}$, which should not only achieve high-order accuracy, but also maintain the essentially non-oscillatory property. The procedure of the reconstruction for the sixth-order case is summarized as follows:

1D reconstruction algorithm:

Step 1. Select a series of central spatial stencils and reconstruct different degree polynomials.

Step 1.1. Reconstruct a zeroth degree polynomial $q_1(x)$ which satisfies

$$\frac{1}{h}\int_{I_k} q_1(x)dx = \overline{u}_k, \quad k = i. \tag{2.8}$$

Step 1.2. Reconstruct a quadratic polynomial $q_2(x)$ which satisfies

$$\frac{1}{h}\int_{I_k} q_2(x)dx = \overline{u}_k, \quad k = i-1, i, i+1. \tag{2.9}$$

Step 1.3. Reconstruct a cubic polynomial $q_3(x)$ which satisfies

$$\frac{1}{h}\int_{I_k} q_3(x)dx = \overline{u}_k, \quad k = i-1, i, i+1; \qquad \frac{1}{h}\int_{I_{k_x}} q_3'(x)dx = \overline{v}_{k_x}, \quad k_x = i. \tag{2.10}$$

Step 1.4. Reconstruct a quintic polynomial $q_4(x)$ which satisfies

$$\frac{1}{h}\int_{I_k} q_4(x)dx = \overline{u}_k,\ k = i-1, i, i+1; \quad \frac{1}{h}\int_{I_{k_x}} q_4'(x)dx = \overline{v}_{k_x},\ k_x = i-1, i, i+1. \tag{2.11}$$

Step 2. Obtain equivalent expressions for above reconstructed polynomials as shown in [29, 30]. To keep consistent notation, we denote $p_1(x) = q_1(x)$ and define

$$p_{l_2}(x) = \frac{1}{\gamma_{l_2,l_2}} q_{l_2}(x) - \sum_{l=1}^{l_2-1} \frac{\gamma_{l,l_2}}{\gamma_{l_2,l_2}} p_l(x), \tag{2.12}$$

with $\sum_{l=1}^{l_2} \gamma_{l,l_2} = 1, \gamma_{l_2,l_2} \neq 0, l_2 = 2, 3, 4$, where these γ_{l_1,l_2} for $l_1 = 1, ..., l_2; l_2 = 2, 3, 4$ are the linear weights and are defined as

$$\gamma_{l_1,l_2} = \frac{\overline{\gamma}_{l_1,l_2}}{\sum_{l=1}^{l_2} \overline{\gamma}_{l,l_2}}; \quad \overline{\gamma}_{l_1,l_2} = 10^{l_1-1}; \quad l_1 = 1, ..., l_2;\ l_2 = 2, 3, 4. \tag{2.13}$$

For example, we take $\overline{\gamma}_{1,4} = 1$, $\overline{\gamma}_{2,4} = 10$, $\overline{\gamma}_{3,4} = 100$ and $\overline{\gamma}_{4,4} = 1000$ for our sixth-order approximation. Correspondingly, we obtain $\gamma_{1,4} = \frac{1}{1111}$, $\gamma_{2,4} = \frac{10}{1111}$, $\gamma_{3,4} = \frac{100}{1111}$ and $\gamma_{4,4} = \frac{1000}{1111}$. Putting these linear weights for our sixth-order approximation into (2.12), we obtain

$$\begin{aligned} p_1(x) &= q_1(x), \\ p_2(x) &= \frac{11}{10} q_2(x) - \frac{1}{10} q_1(x), \\ p_3(x) &= \frac{111}{100} q_3(x) - \frac{11}{100} q_2(x), \\ p_4(x) &= \frac{1111}{1000} q_4(x) - \frac{111}{1000} q_3(x). \end{aligned} \tag{2.14}$$

Step 3. Compute the smoothness indicators β_{l_2}, which measure how smooth the functions $p_{l_2}(x)$ are in the interval $I_i = [x_{i-1/2}, x_{i+1/2}]$:

$$\beta_{l_2} = \sum_{\alpha=1}^{\kappa} \int_{I_i} h^{2\alpha-1} \left(\frac{d^\alpha p_{l_2}(x)}{dx^\alpha} \right)^2 dx, \quad l_2 = 2, 3, 4, \tag{2.15}$$

where $\kappa = 2, 3, 5$ for $l_2 = 2, 3, 4$. The only exception is β_1, which is slightly magnified from zero to a positive value as follows:

First, take two stencils $\{I_{i-1}, I_i\}$ and $\{I_i, I_{i+1}\}$ and obtain their associated smoothness indicators

$$\beta_{1L} = (\overline{u}_i - \overline{u}_{i-1})^2, \quad \beta_{1R} = (\overline{u}_{i+1} - \overline{u}_i)^2. \tag{2.16}$$

Then, according to [29], we define the linear weights of these stencils as

$$\overline{\gamma}_{1L} = \begin{cases} 1, & \beta_{1L} \geq \beta_{1R}, \\ 10, & \text{otherwise}, \end{cases} \quad \overline{\gamma}_{1R} = 11 - \overline{\gamma}_{1L}, \tag{2.17}$$

$$\gamma_{1L} = \frac{\overline{\gamma}_{1L}}{\overline{\gamma}_{1L} + \overline{\gamma}_{1R}}, \quad \gamma_{1R} = 1 - \gamma_{1L}. \tag{2.18}$$

Next, we calculate the non-linear weights of these stencils

$$\omega_{1L} = \frac{\overline{\omega}_{1L}}{\overline{\omega}_{1L} + \overline{\omega}_{1R}}, \quad \omega_{1R} = \frac{\overline{\omega}_{1R}}{\overline{\omega}_{1L} + \overline{\omega}_{1R}}, \tag{2.19}$$

$$\overline{\omega}_{1L} = \gamma_{1L}\left(1 + \frac{|\beta_{1R} - \beta_{1L}|^2}{\beta_{1L} + \varepsilon}\right), \quad \overline{\omega}_{1R} = \gamma_{1R}\left(1 + \frac{|\beta_{1R} - \beta_{1L}|^2}{\beta_{1R} + \varepsilon}\right), \tag{2.20}$$

where $\varepsilon = 10^{-10}$ is a small positive number which is used to avoid the denominator of (2.20) to be zero.

Finally, we set

$$\beta_1 = \Big(\omega_{1L}\big(\overline{u}_i - \overline{u}_{i-1}\big) + \omega_{1R}\big(\overline{u}_{i+1} - \overline{u}_i\big)\Big)^2. \tag{2.21}$$

Step 4. Compute the nonlinear weights based on the linear weights and the smoothness indicators. Here we adopt the idea of WENO-Z as shown in [4] with the quantity τ_4 defined as the absolute difference among the smoothness indicators:

$$\tau_4 = \left(\frac{\sum_{l=1}^{3} |\beta_4 - \beta_l|}{3}\right)^2, \tag{2.22}$$

and we define the nonlinear weights as

$$\omega_{l_1,4} = \frac{\overline{\omega}_{l_1,4}}{\sum_{l=1}^{4} \overline{\omega}_{l,4}}, \quad \overline{\omega}_{l_1,4} = \gamma_{l_1,4}\left(1 + \frac{\tau_4}{\beta_{l_1} + \varepsilon}\right), \quad l_1 = 1, ..., 4, \tag{2.23}$$

where $\varepsilon = 10^{-10}$ in all the formulas.

Step 5. The new final reconstruction polynomials of $u_i(x)$ and $v_i(x)$ are defined as

$$u_i(x) = \sum_{l=1}^{4} \omega_{l,4} p_l(x), \quad v_i(x) = q_4'(x). \tag{2.24}$$

Remark 1. In Step 2 above, the choice of $\overline{\gamma}_{l_1,l_2}$ for $l_1 = 1, ..., l_2$ is not unique, that is to say, the choice of the linear weights γ_{l_1,l_2} for $l_1 = 1, ..., l_2$ is also not unique. For example, we can also take $\overline{\gamma}_{l_1,l_2} = 1$ for all $l_1 = 1, ..., l_2$, thus $\gamma_{l_1,l_2} = \frac{1}{l_2}$ for all $l_1 = 1, ..., l_2$. But from our numerical experiments, we find that even though different choices of the linear weights do not affect the order of accuracy in the smooth regions, the bigger the linear weights for higher-degree polynomials, the steeper the shock transitions near the discontinuities. Of course, the gap between these linear weights should not be too large, otherwise it could become too close to the linear interpolation, which could cause oscillations. We must find a balance. Our choice above works well for all our numerical examples.

Remark 2. In Step 3 above, the definition of β_1 is quite different from the other β_l's. This is because if we use the same method to define β_1 as other β_l's, it would be zero. Even though this does not affect the order of accuracy in the smooth regions, it does lead to more smeared discontinuity transitions, especially when the problem contains strong shocks or contact discontinuities. Therefore, we magnify β_1 from zero to a positive value (dictated by the smoothness in the target cell together with one of its neighboring cells) and this works well in our numerical experiments.

Remark 3. In Step 4 above, through a series of Taylor expansion analyses, we can verify that $\beta_4 - \beta_l = O(h^3)$ for $l < 4$, thus $\tau_4 = O(h^6)$ and

$$\begin{aligned} u(x) - u_i(x) &= u(x) - \sum_{l=1}^{4} \omega_{l,4} p_l(x) \\ &= u(x)\left[1 + \sum_{l=1}^{4}(\omega_{l,4} - \gamma_{l,4})\right] - \left[\sum_{l=1}^{4}(\omega_{l,4} - \gamma_{l,4})p_l(x) + \sum_{l=1}^{4}\gamma_{l,4}p_l(x)\right] \\ &= \left[u(x) - \sum_{l=1}^{4}\gamma_{l,4}p_l(x)\right] + \sum_{l=1}^{4}(\omega_{l,4} - \gamma_{l,4})\Big(u(x) - p_l(x)\Big) \\ &= O(h^6) + O(h^6) * O(h) \\ &= O(h^6). \end{aligned} \tag{2.25}$$

According to above Taylor expansion analyses, we find that setting the power of τ_4 as 2 is enough to ensure the expected accuracy in the smooth regions. There is no need to set it to

be 3 as was done in [29].

Remark 4. In Step 5 above, it is easy to see that if we take $\omega_{l,4} = \gamma_{l,4}$ for $l = 1, ..., 4$ in (2.24), then $u_i(x) = q_4(x)$. This fact is important to maintain the order of accuracy. For $v(x)$, only the first-order derivative of the highest-degree polynomial $q_4(x)$ is used, which is easy to apply and saves the cost of calculating the nonlinear weights. The reason that we compute the first derivative $v_i(x)$ directly from $q_4(x)$ without any limiter is that only the information defined on a hierarchy of nested central spatial stencils is used to reconstruct $u_i(x)$ and the information of the first derivative is not used at all in the stencils of the first two layers. Thus even if there is an oscillation associated with $v_i(x)$, its effect on the oscillation in $u_i(x)$ is minimal.

After all these point values on the cell boundaries are obtained, we put them into (2.6). Then we write the semi-discrete scheme (2.5) as an ordinary differential equation system

$$U_t = L(U), \tag{2.26}$$

and discretize (2.26) by a third-order TVD (total variation diminishing) Runge-Kutta method in time

$$\begin{cases} U^{(1)} = U^n + \Delta t L(U^n), \\ U^{(2)} = \frac{3}{4}U^n + \frac{1}{4}U^{(1)} + \frac{1}{4}\Delta t L(U^{(1)}), \\ U^{n+1} = \frac{1}{3}U^n + \frac{2}{3}U^{(2)} + \frac{2}{3}\Delta t L(U^{(2)}), \end{cases} \tag{2.27}$$

to obtain a fully discrete scheme.

2.1.2 Two dimensional case

We then consider the hyperbolic conservation laws (1.1) in two dimensions

$$\begin{cases} u_t + f(u)_x + g(u)_y = 0, \\ u(x, y, 0) = u_0(x, y). \end{cases} \tag{2.28}$$

Let $v = u_x, w = u_y$, and then from (2.28) and its spacial derivatives, we obtain the following equations

$$\begin{cases} u_t + f(u)_x + g(u)_y = 0, \quad u(x, y, 0) = u_0(x, y), \\ v_t + p(u, v)_x + r(u, v)_y = 0, \quad v(x, y, 0) = v_0(x, y), \\ w_t + q(u, w)_x + s(u, w)_y = 0, \quad w(x, y, 0) = w_0(x, y), \end{cases} \tag{2.29}$$

where

$$p(u,v)=f'(u)u_x=f'(u)v,\quad r(u,v)=g'(u)u_x=g'(u)v,$$
$$q(u,w)=f'(u)u_y=f'(u)w,\quad s(u,w)=g'(u)u_y=g'(u)w.$$

For simplicity, we consider a uniform cell mesh $\{(x_{i+1/2},y_{j+1/2})\}$ with the uniform mesh size $h=x_{i+1/2}-x_{i-1/2}=y_{j+1/2}-y_{j-1/2}$ and denote the cell by $I_{ij}=[x_{i-1/2},x_{i+1/2}]\times[y_{j-1/2},y_{j+1/2}]$ and its center by $(x_i,y_j)=\Big(\frac{1}{2}\big(x_{i-1/2}+x_{i+1/2}\big),\frac{1}{2}\big(y_{j-1/2}+y_{j+1/2}\big)\Big)$.

We denote the two-dimensional cell averages of u, v and w as

$$\begin{cases}\tilde{\overline{u}}_{ij}(t)=\frac{1}{h^2}\int_{I_{ij}}u(x,y,t)dxdy,\\ \tilde{\overline{v}}_{ij}(t)=\frac{1}{h^2}\int_{I_{ij}}v(x,y,t)dxdy,\\ \tilde{\overline{w}}_{ij}(t)=\frac{1}{h^2}\int_{I_{ij}}w(x,y,t)dxdy.\end{cases}\tag{2.30}$$

Integrating (2.29) over the target cell I_{ij} to obtain the integral formulation of the conservation laws

$$\begin{aligned}\frac{d\tilde{\overline{u}}_{ij}(t)}{dt}=-\frac{1}{h^2}\Big[&\int_{y_{j-1/2}}^{y_{j+1/2}}f\Big(u\big(x_{i+1/2},y,t\big)\Big)dy-\int_{y_{j-1/2}}^{y_{j+1/2}}f\Big(u\big(x_{i-1/2},y,t\big)\Big)dy+\\&\int_{x_{i-1/2}}^{x_{i+1/2}}g\Big(u\big(x,y_{j+1/2},t\big)\Big)dx-\int_{x_{i-1/2}}^{x_{i+1/2}}g\Big(u\big(x,y_{j-1/2},t\big)\Big)dx\Big],\\
\frac{d\tilde{\overline{v}}_{ij}(t)}{dt}=-\frac{1}{h^2}\Big[&\int_{y_{j-1/2}}^{y_{j+1/2}}p\Big(u\big(x_{i+1/2},y,t\big),v\big(x_{i+1/2},y,t\big)\Big)dy-\\&\int_{y_{j-1/2}}^{y_{j+1/2}}p\Big(u\big(x_{i-1/2},y,t\big),v\big(x_{i-1/2},y,t\big)\Big)dy+\\&\int_{x_{i-1/2}}^{x_{i+1/2}}r\Big(u\big(x,y_{j+1/2},t\big),v\big(x,y_{j+1/2},t\big)\Big)dx-\\&\int_{x_{i-1/2}}^{x_{i+1/2}}r\Big(u\big(x,y_{j-1/2},t\big),v\big(x,y_{j-1/2},t\big)\Big)dx\Big],\\
\frac{d\tilde{\overline{w}}_{ij}(t)}{dt}=-\frac{1}{h^2}\Big[&\int_{y_{j-1/2}}^{y_{j+1/2}}q\Big(u\big(x_{i+1/2},y,t\big),w\big(x_{i+1/2},y,t\big)\Big)dy-\\&\int_{y_{j-1/2}}^{y_{j+1/2}}q\Big(u\big(x_{i-1/2},y,t\big),w\big(x_{i-1/2},y,t\big)\Big)dy+\\&\int_{x_{i-1/2}}^{x_{i+1/2}}s\Big(u\big(x,y_{j+1/2},t\big),w\big(x,y_{j+1/2},t\big)\Big)dx-\\&\int_{x_{i-1/2}}^{x_{i+1/2}}s\Big(u\big(x,y_{j-1/2},t\big),w\big(x,y_{j-1/2},t\big)\Big)dx\Big].\end{aligned}\tag{2.31}$$

We then approximate (2.31) by the following semi-discrete conservative scheme

$$\begin{cases} \frac{d\tilde{u}_{ij}(t)}{dt} = -\frac{1}{h}(\hat{f}_{i+1/2,j} - \hat{f}_{i-1/2,j}) - \frac{1}{h}(\hat{g}_{i,j+1/2} - \hat{g}_{i,j-1/2}), \\ \frac{d\tilde{v}_{ij}(t)}{dt} = -\frac{1}{h}(\hat{p}_{i+1/2,j} - \hat{p}_{i-1/2,j}) - \frac{1}{h}(\hat{r}_{i,j+1/2} - \hat{r}_{i,j-1/2}), \\ \frac{d\tilde{w}_{ij}(t)}{dt} = -\frac{1}{h}(\hat{q}_{i+1/2,j} - \hat{q}_{i-1/2,j}) - \frac{1}{h}(\hat{s}_{i,j+1/2} - \hat{s}_{i,j-1/2}), \end{cases} \tag{2.32}$$

where the numerical fluxes $\{\hat{f}_{i\pm1/2,j}, \hat{p}_{i\pm1/2,j}, \hat{q}_{i\pm1/2,j}\}$ in the x-direction are defined as

$$\begin{cases} \hat{f}_{i\pm1/2,j} = \sum_{l=1}^{\kappa} \varpi_l \hat{f}(u^-_{i\pm1/2,j+\sigma_l}, u^+_{i\pm1/2,j+\sigma_l}), \\ \hat{p}_{i\pm1/2,j} = \sum_{l=1}^{\kappa} \varpi_l \hat{p}(u^-_{i\pm1/2,j+\sigma_l}, u^+_{i\pm1/2,j+\sigma_l}; v^-_{i\pm1/2,j+\sigma_l}, v^+_{i\pm1/2,j+\sigma_l}), \\ \hat{q}_{i\pm1/2,j} = \sum_{l=1}^{\kappa} \varpi_l \hat{q}(u^-_{i\pm1/2,j+\sigma_l}, u^+_{i\pm1/2,j+\sigma_l}; w^-_{i\pm1/2,j+\sigma_l}, w^+_{i\pm1/2,j+\sigma_l}), \end{cases} \tag{2.33}$$

which approximate the integrations of $\{f(u), p(u,v), q(u,w)\}$ in the y-direction along $x = x_{i\pm1/2}$ respectively. The numerical fluxes $\{\hat{g}_{i,j\pm1/2}, \hat{r}_{i,j\pm1/2}, \hat{s}_{i,j\pm1/2}\}$ in the y-direction are defined in the same way, which approximate the integrations of $\{g(u), r(u,v), s(u,w)\}$ in the x-direction along $y = y_{j\pm1/2}$ respectively. Here ϖ_l and σ_l are the weights and nodes of the κ-point Gaussian quadrature in the cell $\left[-\frac{1}{2}, \frac{1}{2}\right]$. The numerical fluxes $\hat{f}(a,b)$, $\hat{p}(a,b;c,d)$, $\hat{q}(a,b;c,d)$ and $\hat{g}(a,b)$, $\hat{r}(a,b;c,d)$, $\hat{s}(a,b;c,d)$ are defined to be the Lax-Friedrichs fluxes as defined in (2.7). $u^{\pm}_{i\pm1/2,j+\sigma_l}$, $v^{\pm}_{i\pm1/2,j+\sigma_l}$, $w^{\pm}_{i\pm1/2,j+\sigma_l}$ and $u^{\pm}_{i+\sigma_l,j\pm1/2}$, $v^{\pm}_{i+\sigma_l,j\pm1/2}$, $w^{\pm}_{i+\sigma_l,j\pm1/2}$ are the reconstructed approximations of $u(x^{\pm}_{i\pm1/2}, y_{j+\sigma_l}, t)$, $v(x^{\pm}_{i\pm1/2}, y_{j+\sigma_l}, t)$, $w(x^{\pm}_{i\pm1/2}, y_{j+\sigma_l}, t)$ and $u(x_{i+\sigma_l}, y^{\pm}_{j\pm1/2}, t)$, $v(x_{i+\sigma_l}, y^{\pm}_{j\pm1/2}, t)$, $w(x_{i+\sigma_l}, y^{\pm}_{j\pm1/2}, t)$ with suitable order of accuracy.

The most important part of the HWENO schemes is still the spatial reconstruction of the point values $\{u^{\pm}_{i\pm1/2,j+\sigma_l}, v^{\pm}_{i\pm1/2,j+\sigma_l}, w^{\pm}_{i\pm1/2,j+\sigma_l}; u^{\pm}_{i+\sigma_l,j\pm1/2}, v^{\pm}_{i+\sigma_l,j\pm1/2}, w^{\pm}_{i+\sigma_l,j\pm1/2}\}$ from the given cell-average values $\{\tilde{\overline{u}}_{ij}, \tilde{\overline{v}}_{ij}, \tilde{\overline{w}}_{ij}\}$ which should not only achieve high-order of accuracy, but also maintain the essentially non-oscillatory property. The procedure of the reconstruction for the sixth-order accuracy case is summarized as follows.

2D reconstruction algorithm:

7	8	9	$j+1$
4	5	6	j
1	2	3	$j-1$
$i-1$	i	$i+1$	

The big stencil and its new labels.

Step 1. Select a series of central spatial stencils and reconstruct different degree polynomials.

Step 1.1. Reconstruct a zeroth degree polynomial $q_1(x,y)$ which satisfies

$$\frac{1}{h^2}\int_{I_k} q_1(x,y)dxdy = \tilde{\overline{u}}_k, \quad k = 5. \tag{2.34}$$

Step 1.2. Reconstruct a quadratic polynomial $q_2(x,y)$ which satisfies

$$\frac{1}{h^2}\int_{I_k} q_2(x,y)dxdy = \tilde{\overline{u}}_k, \quad k = 1,...,9. \tag{2.35}$$

Step 1.3. Reconstruct a cubic polynomial $q_3(x,y)$ which satisfies

$$\begin{aligned}
&\frac{1}{h^2}\int_{I_k} q_3(x,y)dxdy = \tilde{\overline{u}}_k, \quad k = 1,...,9;\\
&\frac{1}{h^2}\int_{I_{k_x}} \frac{\partial q_3(x,y)}{\partial x}dxdy = \tilde{\overline{v}}_{k_x}, \quad k_x = 5;\\
&\frac{1}{h^2}\int_{I_{k_y}} \frac{\partial q_3(x,y)}{\partial y}dxdy = \tilde{\overline{w}}_{k_y}, \quad k_y = 5.
\end{aligned} \tag{2.36}$$

Step 1.4. Reconstruct a quintic polynomial $q_4(x,y)$ which satisfies

$$\begin{aligned}
&\frac{1}{h^2}\int_{I_k} q_4(x,y)dxdy = \tilde{\overline{u}}_k, \quad k = 1,...,9;\\
&\frac{1}{h^2}\int_{I_{k_x}} \frac{\partial q_4(x,y)}{\partial x}dxdy = \tilde{\overline{v}}_{k_x}, \quad k_x = 1,3,4,5,6,7,9;\\
&\frac{1}{h^2}\int_{I_{k_y}} \frac{\partial q_4(x,y)}{\partial y}dxdy = \tilde{\overline{w}}_{k_y}, \quad k_y = 1,2,3,5,7,8,9.
\end{aligned} \tag{2.37}$$

Note that for above quadratic polynomial $q_2(x,y)$, cubic polynomial $q_3(x,y)$ and quintic polynomial $q_4(x,y)$, they all have the same cell average as u on the target cell I_{ij} (to ensure conservation) and match the other conditions in a least square sense as described in [10].

Step 2. Obtain equivalent expressions for the above reconstructed polynomials as shown in [29, 30]. To keep consistent notation, we denote $p_1(x,y) = q_1(x,y)$ and define

$$p_{l_2}(x,y) = \frac{1}{\gamma_{l_2,l_2}}q_{l_2}(x,y) - \sum_{l=1}^{l_2-1}\frac{\gamma_{l,l_2}}{\gamma_{l_2,l_2}}p_l(x,y), \tag{2.38}$$

with $\sum_{l=1}^{l_2}\gamma_{l,l_2} = 1, \gamma_{l_2,l_2} \neq 0, l_2 = 2,3,4$, where these γ_{l_1,l_2} for $l_1 = 1,...,l_2; l_2 = 2,3,4$ are still the linear weights and are defined as (2.13). Putting these linear weights into (2.38), we

can also obtain

$$
\begin{aligned}
p_1(x,y) &= q_1(x,y),\\
p_2(x,y) &= \frac{11}{10}q_2(x,y) - \frac{1}{10}q_1(x,y),\\
p_3(x,y) &= \frac{111}{100}q_3(x,y) - \frac{11}{100}q_2(x,y),\\
p_4(x,y) &= \frac{1111}{1000}q_4(x,y) - \frac{111}{1000}q_3(x,y).
\end{aligned} \tag{2.39}
$$

Step 3. Compute the smoothness indicators β_{l_2}, which measure how smooth the functions $p_{l_2}(x,y)$ are in the cell $I_{ij} = [x_{i-1/2}, x_{i+1/2}] \times [y_{j-1/2}, y_{j+1/2}]$:

$$
\beta_{l_2} = \sum_{|\alpha|=1}^{\kappa} \int_{I_{ij}} |I_{ij}|^{|\alpha|-1} \left(\frac{\partial^{|\alpha|}}{\partial x^{\alpha_x} \partial y^{\alpha_y}} p_{l_2}(x,y) \right)^2 dxdy, \quad l_2 = 2,3,4, \tag{2.40}
$$

where $\alpha = (\alpha_x, \alpha_y)$, $|\alpha| = \alpha_x + \alpha_y$ and $\kappa = 2,3,5$ for $l_2 = 2,3,4$. The only exception is β_1, which is slightly magnified from zero to a positive value as follows:

First, take four stencils $\{I_{i-1,j},\ I_{i,j},\ I_{i,j+1}\}$, $\{I_{i+1,j},\ I_{i,j},\ I_{i,j+1}\}$, $\{I_{i+1,j},\ I_{i,j},\ I_{i,j-1}\}$ and $\{I_{i-1,j},\ I_{i,j},\ I_{i,j-1}\}$ and construct four linear polynomials $p_{1k}(x,y)$ for $k = 1,2,3,4$ which satisfy

$$
\begin{aligned}
&\frac{1}{h^2}\int_{I_k} q_{11}(x,y)dxdy = \tilde{\overline{u}}_k, \quad k = 4,5,8;\\
&\frac{1}{h^2}\int_{I_k} q_{12}(x,y)dxdy = \tilde{\overline{u}}_k, \quad k = 5,6,8;\\
&\frac{1}{h^2}\int_{I_k} q_{13}(x,y)dxdy = \tilde{\overline{u}}_k, \quad k = 2,5,6;\\
&\frac{1}{h^2}\int_{I_k} q_{14}(x,y)dxdy = \tilde{\overline{u}}_k, \quad k = 2,4,5.
\end{aligned} \tag{2.41}
$$

Their associated smoothness indicators are

$$
\begin{aligned}
\beta_{11} &= (-\tilde{\overline{u}}_{i-1,j} + \tilde{\overline{u}}_{i,j})^2 + (\tilde{\overline{u}}_{i,j+1} - \tilde{\overline{u}}_{i,j})^2,\\
\beta_{12} &= (\tilde{\overline{u}}_{i+1,j} - \tilde{\overline{u}}_{i,j})^2 + (\tilde{\overline{u}}_{i,j+1} - \tilde{\overline{u}}_{i,j})^2,\\
\beta_{13} &= (\tilde{\overline{u}}_{i+1,j} - \tilde{\overline{u}}_{i,j})^2 + (-\tilde{\overline{u}}_{i,j-1} + \tilde{\overline{u}}_{i,j})^2,\\
\beta_{14} &= (-\tilde{\overline{u}}_{i-1,j} + \tilde{\overline{u}}_{i,j})^2 + (-\tilde{\overline{u}}_{i,j-1} + \tilde{\overline{u}}_{i,j})^2.
\end{aligned} \tag{2.42}
$$

Then, according to [30], define the linear weights of these stencils as

$$\overline{\gamma}_{1k} = 1, \quad \gamma_{1k} = \frac{\overline{\gamma}_{1k}}{\sum_{l=1}^{4} \overline{\gamma}_{1l}} = \frac{1}{4}, \quad k = 1, 2, 3, 4. \tag{2.43}$$

The nonlinear weights of these stencils are calculated as

$$\omega_{1k} = \frac{\overline{\omega}_{1k}}{\sum_{l=1}^{4} \overline{\omega}_{1l}}, \quad \overline{\omega}_{1k} = \gamma_{1k} \left(1 + \frac{\tau_1}{\beta_{1k} + \varepsilon} \right), \quad k = 1, 2, 3, 4, \tag{2.44}$$

where the quantity τ_1 is defined as the absolute difference among these smoothness indicators:

$$\tau_1 = \left(\frac{\sum_{k \neq l} |\beta_{1k} - \beta_{1l}|}{6} \right)^2, \tag{2.45}$$

and as before $\varepsilon = 10^{-10}$.

Finally, we set

$$\beta_1 = \sum_{|\alpha|=1} |I_{ij}|^{|\alpha|} \left(\frac{\partial^{|\alpha|}}{\partial x^{\alpha_x} \partial y^{\alpha_y}} \sum_{l=1}^{4} \omega_{1l} p_{1l}(x, y) \right)^2, \tag{2.46}$$

where $\alpha = (\alpha_x, \alpha_y)$, $|\alpha| = \alpha_x + \alpha_y$.

Step 4. Compute the nonlinear weights based on the linear weights and the smoothness indicators. Here we still adopt the idea of WENO-Z with the quantity τ_4 defined as the absolute difference among the smoothness indicators:

$$\tau_4 = \left(\frac{\sum_{l=1}^{3} |\beta_4 - \beta_l|}{3} \right)^2, \tag{2.47}$$

and we define the the non-linear weights as

$$\omega_{l_1,4} = \frac{\overline{\omega}_{l_1,4}}{\sum_{l=1}^{4} \overline{\omega}_{l,4}}, \quad \overline{\omega}_{l_1,4} = \gamma_{l_1,4} \left(1 + \frac{\tau_4}{\beta_{l_1} + \varepsilon} \right), \quad l_1 = 1, ..., 4, \tag{2.48}$$

where $\varepsilon = 10^{-10}$ in all the formulas.

Step 5. The new final reconstruction polynomials of $u_{ij}(x, y)$, $v_{ij}(x, y)$ and $w_{ij}(x, y)$ are defined as

$$\begin{aligned} u_{ij}(x, y) &= \sum_{l=1}^{4} \omega_{l,4} p_l(x, y), \\ v_{ij}(x, y) = \frac{\partial}{\partial x} q_4(x, y), &\quad w_{ij}(x, y) = \frac{\partial}{\partial y} q_4(x, y). \end{aligned} \tag{2.49}$$

Remark 5. *In Step 2 above, in comparison to the classical finite volume HWENO schemes in which the linear weights for HWENO reconstruction are dependent on the quadrature points, we use only one set of the linear weights for the HWENO reconstruction at all Gaussian quadrature points in this paper, thus we can reduce the cost of the spatial reconstruction procedure.*

Just as what we did for the one dimensional case, after all these Gaussian quadrature point values on the boundaries are obtained, we put them into (2.33). Then we write the semi-discrete scheme (2.32) as an ordinary differential equation system (2.26) and discretize it by the third-order TVD Runge-Kutta method (2.27) in time to obtain a fully discrete scheme.

2.2 Finite difference multi-resolution HWENO schemes

2.2.1 One dimensional case

We now design the finite difference multi-resolution HWENO schemes for one dimensional hyperbolic conservation laws (2.1). We discrete the computational domain as before and approximate (2.2) by conservative finite difference schemes

$$\begin{cases} \frac{du_i(t)}{dt} = -\frac{1}{h}(\hat{f}_{i+1/2} - \hat{f}_{i-1/2}), \\ \frac{dv_i(t)}{dt} = -\frac{1}{h}(\hat{g}_{i+1/2} - \hat{g}_{i-1/2}), \end{cases} \tag{2.50}$$

where $u_i(t)$ and $v_i(t)$ are the numerical approximations to the point values $u(x_i, t)$ and $v(x_i, t)$ respectively, and the numerical fluxes

$$\begin{cases} \hat{f}_{i+1/2} = \hat{f}(u_{i-r}, ..., u_{i+s}), \\ \hat{g}_{i+1/2} = \hat{g}(u_{i-r}, ..., u_{i+s}; v_{i-r}, ..., v_{i+s}), \end{cases} \tag{2.51}$$

satisfy the general conditions, such as Lipschitz continuity and consistency with the physical fluxes.

To maintain stability, we also need to consider the upwind property of the scheme. Thus, we split the fluxes $f(u)$ and $g(u, v)$ into two parts

$$\begin{cases} f(u) = f^+(u) + f^-(u), \quad \frac{d}{du}f^+(u) \geq 0, \quad \frac{d}{du}f^-(u) \leq 0, \\ g(u, v) = g^+(u, v) + g^-(u, v), \quad \frac{d}{dv}g^+(u, v) \geq 0, \quad \frac{d}{dv}g^-(u, v) \leq 0, \end{cases} \tag{2.52}$$

where

$$\begin{cases} f^{\pm}(u) = \frac{1}{2}\Big(f(u) \pm \alpha u\Big), \\ g^{\pm}(u,v) = \frac{1}{2}\Big(g(u,v) \pm \alpha v\Big), \end{cases} \tag{2.53}$$

with $\alpha = \max_u |f'(u)|$ over the whole range of u. Take $\overline{u}_i = f^+(u_i)$, $\overline{v}_i = g^+(u_i, v_i)$, and repeat the 1D reconstruction algorithm in Section 2.1.1 to obtain $\hat{f}^+_{i+1/2} = u^-_{i+1/2}$, $\hat{g}^+_{i+1/2} = v^-_{i+1/2}$. Likewise, take $\overline{u}_i = f^-(u_i)$, $\overline{v}_i = g^-(u_i, v_i)$, and repeat the 1D reconstruction algorithm in Section 2.1.1 to obtain $\hat{f}^-_{i+1/2} = u^+_{i+1/2}$, $\hat{g}^-_{i+1/2} = v^+_{i+1/2}$. Then the numerical fluxes are given by

$$\begin{cases} \hat{f}_{i+1/2} = \hat{f}^+_{i+1/2} + \hat{f}^-_{i+1/2}, \\ \hat{g}_{i+1/2} = \hat{g}^+_{i+1/2} + \hat{g}^-_{i+1/2}. \end{cases} \tag{2.54}$$

After all these numerical fluxes on the cell boundaries are obtained, we discretize the ordinary differential equation system (2.26) of the semi-discrete scheme (2.50) by the third-order TVD Runge-Kutta method (2.27) to advance in time.

2.2.2 Two dimensional case

While the finite difference scheme has comparable cost and performance as the finite volume scheme in one dimension, in two dimensions the finite difference scheme is simpler and more cost-effective than the finite volume scheme, as we can perform differentiations dimension by dimension, but integrals must be performed in two dimensional cells. To be more specific, we describe in detail the design of the finite difference multi-resolution HWENO schemes for two dimensional hyperbolic conservation laws (2.28). With the same discretization of the computational domain as before, we approximate (2.29) by

$$\begin{cases} \frac{du_{ij}(t)}{dt} = -\frac{1}{h}(\hat{f}_{i+1/2,j} - \hat{f}_{i-1/2,j}) - \frac{1}{h}(\hat{g}_{i,j+1/2} - \hat{g}_{i,j-1/2}), \\ \frac{dv_{ij}(t)}{dt} = -\frac{1}{h}(\hat{p}_{i+1/2,j} - \hat{p}_{i-1/2,j}) - \frac{1}{h}(\hat{r}_{i,j+1/2} - \hat{r}_{i,j-1/2}), \\ \frac{dw_{ij}(t)}{dt} = -\frac{1}{h}(\hat{q}_{i+1/2,j} - \hat{q}_{i-1/2,j}) - \frac{1}{h}(\hat{s}_{i,j+1/2} - \hat{s}_{i,j-1/2}), \end{cases} \tag{2.55}$$

where $u_{ij}(t)$, $v_{ij}(t)$ and $w_{ij}(t)$ are the numerical approximations to the point values $u(x_i, y_j, t)$, $v(x_i, y_j, t)$ and $w(x_i, y_j, t)$ respectively and the numerical fluxes $\hat{f}_{i\pm1/2,j}$, $\hat{p}_{i\pm1/2,j}$, $\hat{g}_{i,j\pm1/2}$ and $\hat{s}_{i,j\pm1/2}$ are reconstructed by the method straightforwardly extended from the one-dimensional method in a dimension-by-dimension manner. The only exception is the re-

construction of $\hat{q}_{i\pm1/2,j}$ and $\hat{r}_{i,j\pm1/2}$ for the mixed derivative quantities $f(u)_{yx}$ and $g(u)_{xy}$ respectively.

2D reconstruction algorithm of the mixed derivative quantities:

Step 1. Flux splitting.

Firstly, split the fluxes into two parts

$$\begin{cases} q(u,w) = q^+(u,w) + q^-(u,w), & \frac{d}{dw}q^+(u,w) \geq 0, \quad \frac{d}{dw}q^-(u,w) \leq 0, \\ r(u,v) = r^+(u,v) + r^-(u,v), & \frac{d}{dv}r^+(u,v) \geq 0, \quad \frac{d}{dv}r^-(u,v) \leq 0, \end{cases} \tag{2.56}$$

where

$$\begin{cases} q^\pm(u,w) = \frac{1}{2}\Big(q\big(u,w\big) \pm \alpha w\Big), \\ r^\pm(u,v) = \frac{1}{2}\Big(r\big(u,v\big) \pm \alpha v\Big), \end{cases} \tag{2.57}$$

where $\alpha = \max_u |f'(u)|$ over the whole range of u.

Step 2. Reconstruction of $\{\hat{q}^\pm_{i+1/2,j},\, \hat{r}^\pm_{i,j+1/2}\}$.

Secondly, choose a stencil $\{I_{i-1,j}, I_{i,j}, I_{i+1,j}\}$ at $y = y_j$ and interpolate a quadratic polynomial $Q(x)$ which satisfies

$$\frac{1}{h}\int_{I_{k,j}} Q(x)dx = q^+_{k,j}, \quad k = i-1, i, i+1, \tag{2.58}$$

then the approximation of $q^+(x_{i+1/2}, y_j)$ is

$$\hat{q}^+_{i+1/2,j} \approx Q(x^-_{i+1/2}) = -\frac{1}{6}q^+_{i-1,j} + \frac{5}{6}q^+_{i,j} + \frac{1}{3}q^+_{i+1,j}. \tag{2.59}$$

As for $\hat{q}^-_{i+1/2,j}$, the reconstruction procedure is mirror symmetric with respect to $x_{i+1/2}$ of that for $\hat{q}^+_{i+1/2,j}$ above

$$\hat{q}^-_{i+1/2,j} \approx Q(x^+_{i+1/2}) = \frac{1}{3}q^-_{i,j} + \frac{5}{6}q^-_{i+1,j} - \frac{1}{6}q^-_{i+2,j}. \tag{2.60}$$

The reconstruction of $\hat{r}^\pm_{i,j+1/2}$ in the y-direction is similar.

Step 3. Calculation of the numerical fluxes.

Finally, we obtain the numerical fluxes $\hat{q}_{i+1/2,j}$ and $\hat{r}_{i,j+1/2}$ as

$$\begin{cases} \hat{q}_{i+1/2,j} = \hat{q}^+_{i+1/2,j} + \hat{q}^-_{i+1/2,j}, \\ \hat{r}_{i,j+1/2} = \hat{r}^+_{i,j+1/2} + \hat{r}^-_{i,j+1/2}. \end{cases} \tag{2.61}$$

Remark 6. We would like to mention that we have tried many methods to treat the mixed derivatives, but have encountered a common difficulty that they are all unstable except for the method described above. A significant drawback of the method described above is that the accuracy is now limited to fourth order. It would be interesting to obtain a stable sixth-order discretization for these mixed derivatives in the finite difference setting.

Remark 7. For the systems, the reconstruction is performed in the local characteristic directions to avoid oscillations near the discontinuities, see [21] for details.

Finally just as what we did for the one dimensional case, after all these numerical fluxes on the cell boundaries are obtained, we discretize the ordinary differential equation system (2.26) of the semi-discrete scheme (2.55) by the third-order TVD Runge-Kutta method (2.27) to advance in time.

3 Numerical tests

In this section, we present a number of typical experiments to test the performances of the finite volume and finite difference multi-resolution HWENO schemes which are termed as HWENOκ-FV and HWENOκ-FD respectively where κ is the order of the scheme. For all the numerical tests in this paper, the third-order Runge-Kutta method (2.27) is used in time, and the CFL number is set as 0.6 for all the one and two dimensional cases, except for the accuracy tests where a suitably reduced time step is used to guarantee the dominance of the spatial error. As mentioned before, we take the linear weights as $\overline{\gamma}_{1,4} = 1$, $\overline{\gamma}_{2,4} = 10$, $\overline{\gamma}_{3,4} = 100$ and $\overline{\gamma}_{4,4} = 1000$ for both the finite volume and finite difference schemes in the one and two dimensions in this paper.

Example 3.1. First, we solve the following one-dimensional nonlinear scalar Burgers' equation:

$$\mu_t + \left(\frac{\mu^2}{2}\right)_x = 0, \quad 0 < x < 2, \tag{3.1}$$

with the initial condition $\mu(x, 0) = 0.5 + \sin(\pi x)$ and periodic boundary condition. When $t = 0.5/\pi$, the solution is still smooth, and the corresponding errors and orders by HWENO6-

FV and HWENO6-FD schemes are listed in Table 3.1. When $t = 1.5/\pi$, the solution is discontinuous, and the corresponding numerical solutions obtained by HWENO6-FV and HWENO6-FD schemes are plotted in Fig 3.1 against the reference exact solution.

Table 3.1: $\mu_t + \left(\frac{\mu^2}{2}\right)_x = 0$. The initial condition $\mu(x,0) = 0.5 + \sin(\pi x)$. Periodic boundary condition. $T = 0.5/\pi$. HWENO6-FV and HWENO6-FD schemes. L^1 and L^∞.

	HWENO6-FV scheme				HWENO6-FD scheme			
grid points	L^1 error	order	L^∞ error	order	L^1 error	order	L^∞ error	order
100	9.87E-09		1.34E-07		8.18E-09		1.05E-07	
120	3.21E-09	6.16	4.72E-08	5.73	2.34E-09	6.88	3.69E-08	5.72
140	1.29E-09	5.91	1.93E-08	5.79	8.41E-10	6.63	1.17E-08	7.43
160	5.71E-10	6.11	8.88E-09	5.83	3.55E-10	6.47	5.41E-09	5.79
180	2.84E-10	5.92	4.46E-09	5.86	1.68E-10	6.35	2.71E-09	5.87
200	1.52E-10	5.92	2.40E-09	5.88	8.76E-11	6.17	1.45E-09	5.91

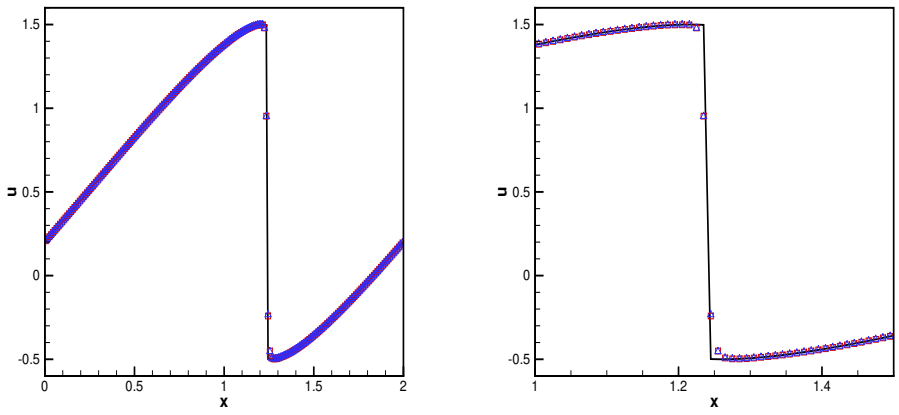

Figure 3.1: 1D-Burgers' equation. $T = 1.5/\pi$. Left: the numerical and exact solutions; right: the numerical and exact solutions zoomed in. Solid line: the exact solution; triangles: the result of HWENO6-FV scheme; squares: the result of HWENO6-FD scheme. Number of cells: 200.

Example 3.2. Next, we solve the following two-dimensional nonlinear scalar Burgers' equation:

$$\mu_t + \left(\frac{\mu^2}{2}\right)_x + \left(\frac{\mu^2}{2}\right)_y = 0, \quad 0 < x, y < 4, \tag{3.2}$$

with the initial condition $\mu(x,y,0) = 0.5+\sin\left(\pi(x+y)/2\right)$ and periodic boundary condition. When $t = 0.5/\pi$, the solution is still smooth, and the corresponding errors and orders by HWENO6-FV and HWENO4-FD schemes are listed in Table 3.2. When $t = 1.5/\pi$, the solution is discontinuous, and the corresponding numerical solutions at $x = y$ obtained by HWENO6-FV and HWENO4-FD schemes are plotted in Fig 3.2 against the reference exact solution.

Table 3.2: $\mu_t + \left(\frac{\mu^2}{2}\right)_x + \left(\frac{\mu^2}{2}\right)_y = 0$. The initial condition $\mu(x,y,0) = 0.5+\sin\left(\pi(x+y)/2\right)$. Periodic boundary condition. $T = 0.5/\pi$. HWENO6-FV and HWENO4-FD schemes. L^1 and L^∞.

	HWENO6-FV scheme				HWENO4-FD scheme			
grid points	L^1 error	order	L^∞ error	order	L^1 error	order	L^∞ error	order
100×100	1.01E-07		1.49E-06		1.45E-06		1.42E-05	
120×120	3.68E-08	5.53	5.57E-07	5.38	6.97E-07	4.00	7.15E-06	3.76
140×140	1.54E-08	5.65	2.38E-07	5.51	3.77E-07	3.99	3.93E-06	3.88
160×160	7.13E-09	5.78	1.13E-07	5.60	2.20E-07	4.03	2.31E-06	3.99
180×180	3.67E-09	5.65	5.79E-08	5.66	1.36E-07	4.05	1.43E-06	4.05
200×200	2.00E-09	5.76	3.17E-08	5.71	8.89E-08	4.07	9.37E-07	4.03

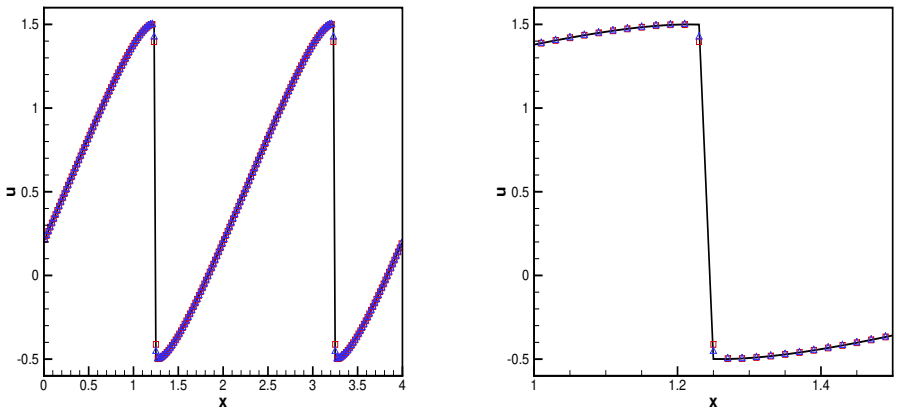

Figure 3.2: 2D-Burgers' equation. $T = 1.5/\pi$. Left: the numerical and exact solutions at $x = y$; right: the numerical and exact solutions at $x = y$ zoomed in. Solid line: the exact solution; triangles: the result of HWENO6-FV scheme; squares: the result of HWENO4-FD scheme. Number of cells: 200×200.

Example 3.3. Then, we solve the following one-dimensional compressible Euler equations:

$$\frac{\partial}{\partial t}\begin{pmatrix}\rho\\ \rho\mu\\ E\end{pmatrix}+\frac{\partial}{\partial x}\begin{pmatrix}\rho\mu\\ \rho\mu^2+p\\ \mu(E+p)\end{pmatrix}=0,\quad 0<x<2\pi, \tag{3.3}$$

where ρ is the density, μ is the velocity, E is the total energy and p is the pressure. The initial conditions are

$$\rho(x,0)=\tfrac{1+0.2\sin(x)}{2\sqrt{3}},\quad \mu(x,0)=\sqrt{\gamma}\rho(x,0),\quad p(x,0)=\rho(x,0)^{\gamma}. \tag{3.4}$$

The boundary conditions are periodic. Under above initial conditions, boundary conditions and special choice of the parameter $\gamma=3$, we can prove that $2\sqrt{3}\rho(x,t)$ is the exact solution of the following Burgers' equation:

$$\begin{cases}\mu_t+\left(\frac{\mu^2}{2}\right)_x=0,\quad 0<x<2\pi,\\ \mu(x,0)=1+0.2\sin(x),\end{cases} \tag{3.5}$$

and the corresponding velocity and pressure satisfy

$$\mu(x,t)=\sqrt{\gamma}\rho(x,t),\quad p(x,t)=\rho(x,t)^{\gamma}. \tag{3.6}$$

It is easy to verify that the solution of the above Burgers' equation is smooth until time $T=5$. We compute the solution up to $T=3$, and the corresponding errors and orders by HWENO6-FV and HWENO6-FD schemes are listed in Table 3.3.

Table 3.3: 1D-Euler equations: The initial condition $\rho(x,0)=\frac{1+0.2\sin(x)}{2\sqrt{3}}$, $\mu(x,0)=\sqrt{\gamma}\rho(x,0)$ and $p(x,0)=\rho(x,0)^{\gamma}$. Periodic boundary condition. $T=3$. HWENO6-FV and HWENO6-FD schemes. L^1 and L^∞.

	HWENO6-FV scheme				HWENO6-FD scheme			
grid points	L^1 error	order	L^∞ error	order	L^1 error	order	L^∞ error	order
100	3.20E-08		7.37E-07		3.36E-08		7.87E-07	
120	1.15E-08	5.63	2.67E-07	5.57	1.19E-08	5.69	2.84E-07	5.58
140	4.85E-09	5.59	1.21E-07	5.13	5.06E-09	5.54	1.26E-07	5.27
160	2.28E-09	5.66	5.48E-08	5.93	2.36E-09	5.72	5.75E-08	5.89
180	1.17E-09	5.65	2.97E-08	5.21	1.20E-09	5.70	3.06E-08	5.35
200	6.35E-10	5.81	1.56E-08	6.08	6.51E-10	5.84	1.63E-08	6.00

Example 3.4. Next, we solve the following two-dimensional compressible Euler equations:

$$\frac{\partial}{\partial t}\begin{pmatrix}\rho\\ \rho\mu\\ \rho\nu\\ E\end{pmatrix}+\frac{\partial}{\partial x}\begin{pmatrix}\rho\mu\\ \rho\mu^2+p\\ \rho\mu\nu\\ \mu(E+p)\end{pmatrix}+\frac{\partial}{\partial y}\begin{pmatrix}\rho\nu\\ \rho\mu\nu\\ \rho\nu^2+p\\ \nu(E+p)\end{pmatrix}=0,\quad 0<x,y<4\pi, \tag{3.7}$$

where ρ is the density, μ is the velocity in the x-direction, ν is the velocity in the y-direction, E is the total energy and p is the pressure. The initial conditions are

$$\rho(x,y,0)=\frac{1+0.2\sin(\frac{x+y}{2})}{\sqrt{6}},\ \mu(x,y,0)=\nu(x,y,0)=\sqrt{\tfrac{\gamma}{2}}\rho(x,y,0),\ p(x,y,0)=\rho(x,y,0)^\gamma. \tag{3.8}$$

The boundary conditions are periodic in both directions. Under above initial conditions, boundary conditions and special choice of the parameter $\gamma=3$, we can prove that $\sqrt{6}\rho(x,y,t)$ is the exact solution of the following Burgers' equation:

$$\begin{cases}\mu_t+\left(\frac{\mu^2}{2}\right)_x+\left(\frac{\mu^2}{2}\right)_y=0,\quad 0<x,y<4\pi,\\ \mu(x,y,0)=1+0.2\sin(\frac{x+y}{2}),\end{cases} \tag{3.9}$$

and the corresponding velocity and pressure satisfy

$$\mu(x,y,t)=\nu(x,y,t)=\sqrt{\tfrac{\gamma}{2}}\rho(x,y,t),\quad p(x,y,t)=\rho(x,y,t)^\gamma. \tag{3.10}$$

It is easy to verify that the solution of the above Burgers' equation is smooth until time $T=5$. We compute the solution up to $T=3$, and the corresponding errors and orders by HWENO6-FV and HWENO4-FD schemes are listed in Table 3.4.

Example 3.5. Consider the isentropic vortex problem [21] for the two-dimensional compressible Euler equations (3.7). The mean flow is $\rho=p=u=v=1$. We add an isentropic vortex perturbation centered at (x_0,y_0) in (u,v) and $T=p/\rho$, with no perturbation in $S=p/\rho^\gamma$ to the mean flow,

$$(\delta u,\delta v)=\frac{\epsilon}{2\pi}e^{0.5(1-r^2)}(-\bar{y},\bar{x}),\quad \delta T=\frac{(\gamma-1)\epsilon^2}{8\gamma\pi^2}e^{1-r^2} \tag{3.11}$$

where $(\bar{x},\bar{y})=(x-x_0,y-y_0), r^2=\bar{x}^2+\bar{y}^2$. The exact solution is the passive convection of the vortex with the mean velocity. The domain is taken as $[-10,10]\times[-10,10]$ and

Table 3.4: 2D-Euler equations: The initial condition $\rho(x,y,0) = \frac{1+0.2\sin(\frac{x+y}{2})}{\sqrt{6}}$, $\mu(x,y,0) = \nu(x,y,0) = \sqrt{\frac{\gamma}{2}}\rho(x,y,0)$ and $p(x,y,0) = \rho(x,y,0)^\gamma$. Periodic boundary condition. $T = 3$. HWENO6-FV and HWENO4-FD schemes. L^1 and L^∞.

	HWENO6-FV scheme				HWENO4-FD scheme			
grid points	L^1 error	order	L^∞ error	order	L^1 error	order	L^∞ error	order
100×100	7.24E-07		1.45E-05		7.27E-06		1.05E-04	
120×120	2.90E-07	5.01	6.35E-06	4.54	3.71E-06	3.69	5.83E-05	3.24
140×140	1.29E-07	5.26	2.98E-06	4.91	2.10E-06	3.71	3.38E-05	3.54
160×160	6.28E-08	5.40	1.46E-06	5.36	1.27E-06	3.76	2.08E-05	3.62
180×180	3.41E-08	5.19	8.21E-07	4.86	8.11E-07	3.81	1.37E-05	3.58
200×200	1.94E-08	5.37	4.56E-07	5.58	5.43E-07	3.81	9.15E-06	3.81

$(x_0, y_0) = (0, 0)$. The boundary conditions are periodic in both directions. We set $\gamma = 1.4$ and the vortex strength $\epsilon = 1.0$. We compute the solution up to $T = 5$, and the corresponding errors and orders by HWENO6-FV and HWENO4-FD schemes are listed in Table 3.5.

Table 3.5: The isentropic vortex problem: The initial condition $\rho(x,y,0) = (1 - \frac{(\gamma-1)\epsilon^2}{8\gamma\pi^2}e^{1-r^2})^{\frac{1}{\gamma-1}}$, $(\mu(x,y,0), \nu(x,y,0)) = 1 + \frac{\epsilon}{2\pi}e^{0.5(1-r^2)}(-\bar{y}, \bar{x})$ and $p(x,y,0) = \rho(x,y,0)^\gamma$. Periodic boundary condition. $T = 5$. HWENO6-FV and HWENO4-FD schemes. L^1 and L^∞.

	HWENO6-FV scheme				HWENO4-FD scheme			
grid points	L^1 error	order	L^∞ error	order	L^1 error	order	L^∞ error	order
100×100	2.98E-07		3.05E-05		6.80E-06		2.58E-04	
120×120	1.17E-07	5.13	1.22E-05	5.04	3.56E-06	3.55	1.50E-04	2.95
140×140	5.21E-08	5.26	5.33E-06	5.36	2.09E-06	3.46	8.71E-05	3.54
160×160	2.56E-08	5.32	2.57E-06	5.46	1.31E-06	3.52	5.37E-05	3.62
180×180	1.36E-08	5.39	1.36E-06	5.38	8.60E-07	3.54	3.53E-05	3.56
200×200	7.67E-09	5.41	7.57E-07	5.59	5.91E-07	3.56	2.40E-05	3.66

Comment: According to the results listed in above five tables Table 3.1, Table 3.2, Table 3.3, Table 3.4 and Table 3.5, we can see that both the finite volume and finite difference HWENO schemes achieve their designed order of accuracy and that the errors of the finite volume schemes are bigger than those of the finite difference schemes on the same meshes for Example 3.1, while Example 3.3 shows the opposite result. From Fig 3.1 and Fig 3.2,

we can observe that both the finite volume and finite difference HWENO schemes work well in comparison with the exact solutions and there is not much difference between these two schemes.

Example 3.6. The Buckley-Leverett problem: one-dimensional nonlinear non-convex scalar Buckley-Leverett problem:

$$\mu_t + \left(\frac{4\mu^2}{4\mu^2 + (1-\mu)^2} \right)_x = 0, \quad -1 < x < 1, \tag{3.12}$$

with the initial condition:

$$\mu = \begin{cases} 1, & -0.5 < x < 0, \\ 0, & elsewhere. \end{cases} \tag{3.13}$$

We present the computed solutions obtained by HWENO6-FV and HWENO6-FD schemes at $T = 0.4$ in Fig 3.3 against the reference exact solution. The exact solution is a shock-rarefaction-contact discontinuity mixture and some high-order schemes may fail to converge to the correct entropy solution for this problem. From Fig 3.3, we can observe that both the finite volume and finite difference HWENO schemes could converge to the right solution and gain good resolution.

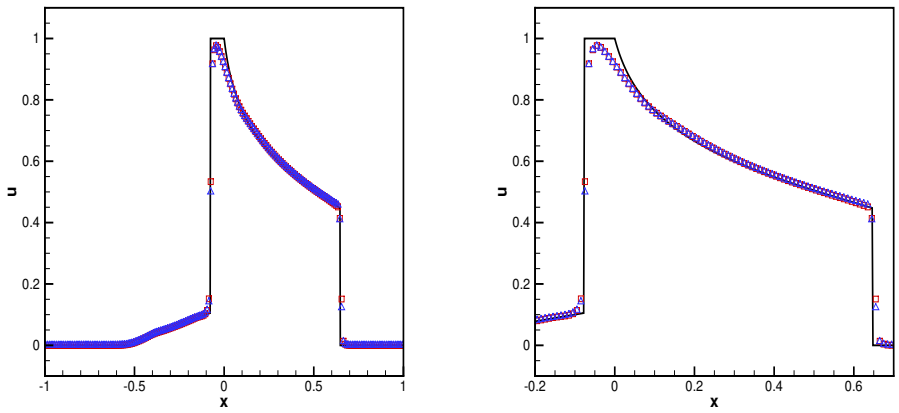

Figure 3.3: The Buckley-Leverett problem. $T = 0.4$. Left: the numerical and exact solutions; right: the numerical and exact solutions zoomed in. Solid line: the exact solution; triangles: the result of HWENO6-FV scheme; squares: the result of HWENO6-FD scheme. Number of cells: 200.

Example 3.7. The Lax problem: one-dimensional compressible Euler equations (3.3) with the Riemann initial condition:

$$(\rho, \mu, p)^T = \begin{cases} (0.445, 0.698, 3.528)^T, & -0.5 < x < 0, \\ (0.5, 0, 0.571)^T, & 0 < x < 0.5. \end{cases} \tag{3.14}$$

We present the computed density ρ obtained by HWENO6-FV and HWENO6-FD schemes at $T = 0.16$ in Fig 3.4 against the reference exact solution.

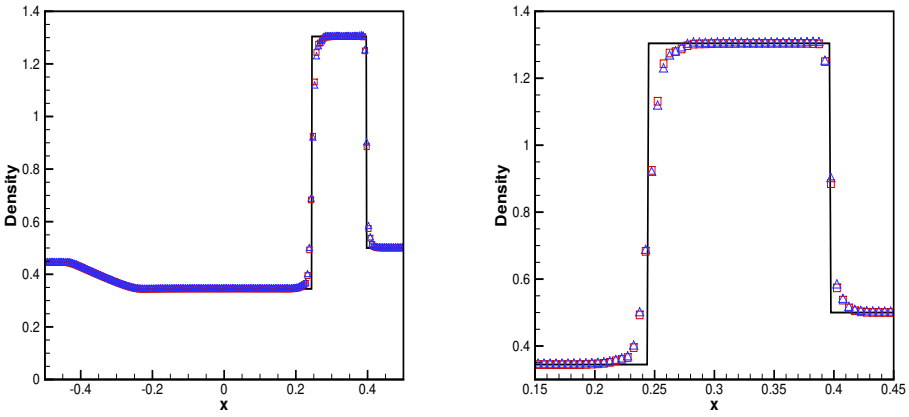

Figure 3.4: The Lax problem. $T = 0.16$. Left: density; right: density zoomed in. Solid line: the exact solution; triangles: the result of HWENO6-FV scheme; squares: the result of HWENO6-FD scheme. Number of cells: 200.

Example 3.8. The shock density wave interaction problem: one-dimensional compressible Euler equations (3.3) with a moving Mach=3 shock interaction with sine waves in density:

$$(\rho, \mu, p)^T = \begin{cases} (3.857143, 2.629369, 10.333333)^T, & -5 < x < -4, \\ \big(1 + 0.2\sin(5x), 0, 1\big)^T, & -4 < x < 5. \end{cases} \tag{3.15}$$

We present the computed density ρ obtained by HWENO6-FV and HWENO6-FD schemes at $T = 1.8$ in Fig 3.5 against the reference "exact" solution which is a converged solution computed by the fifth-order finite difference WENO scheme [12] with 8000 grid points.

Example 3.9. The blast wave problem: one-dimensional compressible Euler equations (3.3) with the initial condition:

$$(\rho, \mu, p)^T = \begin{cases} (1, 0, 10^3)^T, & 0 < x < 0.1, \\ (1, 0, 10^{-2})^T, & 0.1 < x < 0.9, \\ (1, 0, 10^2)^T, & 0.9 < x < 1. \end{cases} \tag{3.16}$$

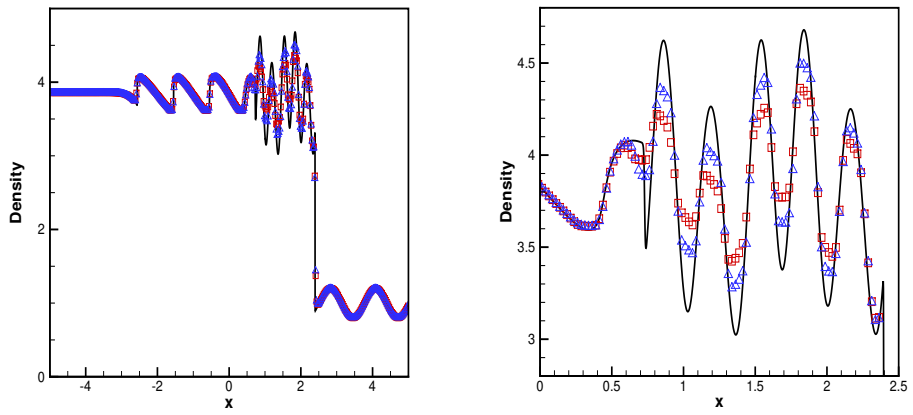

Figure 3.5: The shock density wave interaction problem. $T = 1.8$. Left: density; right: density zoomed in. Solid line: the exact solution; triangles: the result of HWENO6-FV scheme; squares: the result of HWENO6-FD scheme. Number of cells: 400.

We present the computed density ρ obtained by HWENO6-FV and HWENO6-FD schemes at $T = 0.038$ in Fig 3.6 against the reference "exact" solution which is a converged solution computed by the fifth-order finite difference WENO scheme [12] with 16000 grid points.

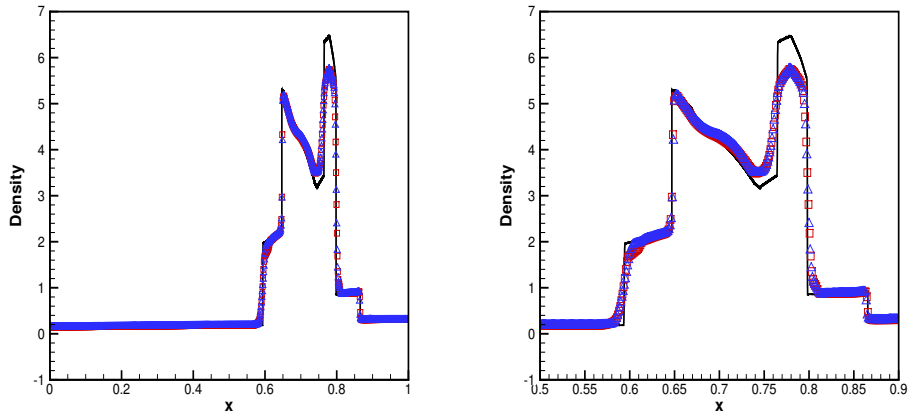

Figure 3.6: The blast wave problem. $T = 0.038$. Left: density; right: density zoomed in. Solid line: the exact solution; triangles: the result of HWENO6-FV scheme; squares: the result of HWENO6-FD scheme. Number of cells: 800.

Example 3.10. The Lax problem: two-dimensional compressible Euler equations (3.7) with

the Riemann initial condition:

$$(\rho, \mu, \nu, p)^T = \begin{cases} (0.445, 0.698, 0, 3.528)^T, & -0.5 < x^{'} < 0, \\ (0.5, 0, 0, 0.571)^T, & 0 < x^{'} < 0.5, \end{cases} \tag{3.17}$$

where $x^{'}$ denotes the x-axis of the new rectangular coordinate system which is obtained by rotating the original rectangular coordinate system counterclockwise by 45 degrees. The similar one-dimensional boundary condition is applied in the $x^{'}$-direction. Since the velocity is zero in the $y^{'}$-direction, all the variables have the same value along $y^{'} = constant$. We present the computed density ρ obtained by HWENO6-FV and HWENO4-FD schemes at $T = 0.16$ along $y = x$ in Fig 3.7 against the reference exact solution.

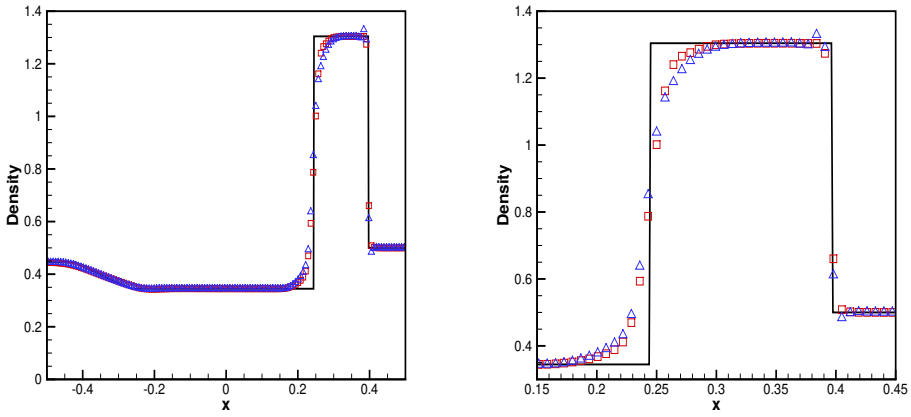

Figure 3.7: The Lax problem. $T = 0.16$. Left: density cut along $y = x$; right: density zoomed in. Solid line: the exact solution; triangles: the result of HWENO6-FV scheme; squares: the result of HWENO4-FD scheme. Number of cells: 142×142 (The grid is selected in this way to compare with the corresponding one-dimensional case, since there is a factor of $\sqrt{2}$ adjustment to achieve effectively equivalent mesh sizes in 1D and in 2D along the diagonal line).

Example 3.11. The shock density wave interaction problem: two-dimensional compressible Euler equations (3.7) with a moving Mach=3 shock interaction with sine waves in density:

$$(\rho, \mu, \nu, p)^T = \begin{cases} (3.857143, 2.629369, 0, 10.333333)^T, & -5 < x^{'} < -4, \\ \left(1 + 0.2\sin(5x^{'}), 0, 0, 1\right)^T, & -4 < x^{'} < 5, \end{cases} \tag{3.18}$$

where $x^{'}$ denotes the x-axis of the new rectangular coordinate system which is obtained by rotating the original rectangular coordinate system counterclockwise by 45 degrees. The

similar one-dimensional boundary condition is applied in the $x^{'}$-direction. Since the velocity is zero in the $y^{'}$-direction, all the variables have the same value along $y^{'} = constant$. We present the computed density ρ obtained by HWENO6-FV and HWENO4-FD schemes at $T = 1.8$ along $y = x$ in Fig 3.8 against the reference "exact" solution which is a converged solution computed by the fifth-order finite difference WENO scheme [12] with 8000 grid points.

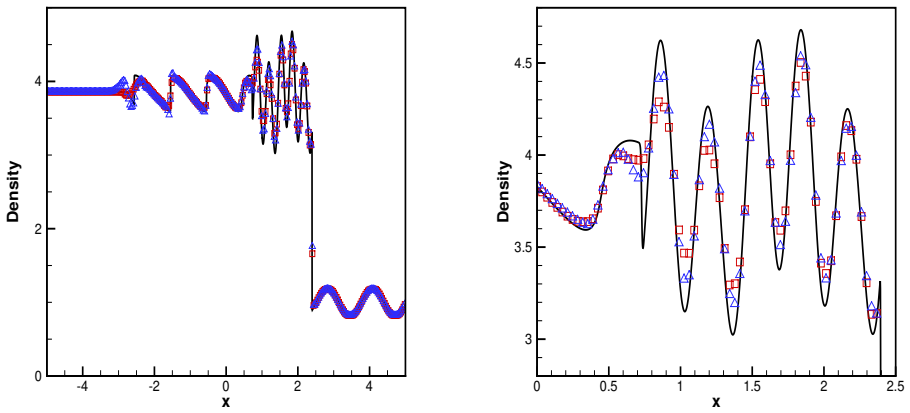

Figure 3.8: The shock density wave interaction problem. $T = 1.8$. Left: density cut along $y = x$; right: density zoomed in. Solid line: the exact solution; triangles: the result of HWENO6-FV scheme; squares: the result of HWENO4-FD scheme. Number of cells: 283×283 (The grid is selected in this way to compare with the corresponding one-dimensional case, since there is a factor of $\sqrt{2}$ adjustment to achieve effectively equivalent mesh sizes in 1D and in 2D along the diagonal line).

Example 3.12. Double Mach reflection problem: two-dimensional compressible Euler equations (3.7) in a computational domain $[0, 4]\times[0, 1]$ with a reflection wall lying at the bottom of the domain starting from $x = \frac{1}{6}$, $y = 0$, making a 60° angle with the x-axis. For the bottom of the domain, the reflection boundary condition is used at the reflection wall, and the exact post-shock condition is imposed at the rest of the bottom boundary (the part from $x = 0$ to $x = \frac{1}{6}$). For the top of the domain, the boundary is the exact motion of the Mach 10 shock with $\gamma = 1.4$. We present the computed density ρ obtained by HWENO6-FV and HWENO4-FD schemes at $t = 0.2$ in the region of $[0, 3]\times[0, 1]$ in Fig 3.9 and the blow-up

region around the double Mach stem in Fig 3.10.

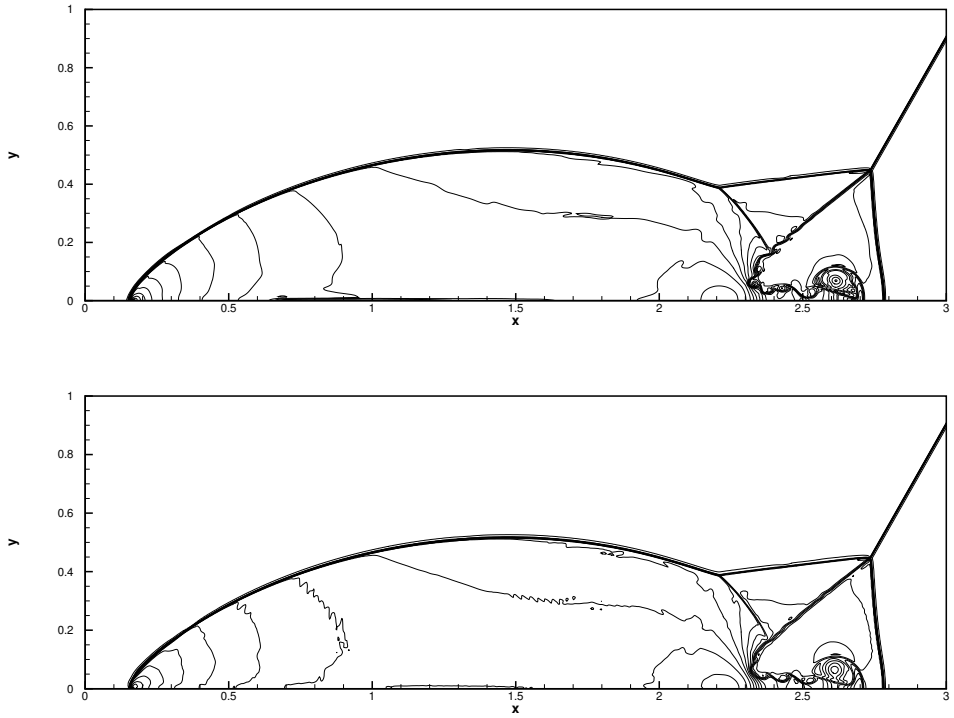

Figure 3.9: Double Mach reflection problem. $T = 0.2$. 30 equally spaced density contours from 1.5 to 22.7. Top: HWENO6-FV; bottom: HWENO4-FD. Number of cells: 1600×400 in the region of $[0, 4]\times[0, 1]$.

Example 3.13. Forward step problem: two-dimensional compressible Euler equations (3.7) in a Mach 3 wind tunnel with a step. The wind tunnel is one length unit wide and three length units long with a 0.2 length units high step located 0.6 length units from the left-side end of the tunnel. The problem is initialized by a right-going Mach 3 flow at the beginning. The reflection boundary condition is used along the wall of the tunnel, the inflow boundary condition is imposed at the entrance, and the outflow boundary condition is imposed at the exit. We present the computed density ρ obtained by HWENO6-FV and HWENO4-FD schemes at $t = 4$ in the region of $[0, 3]\times[0, 1]$ in Fig 3.11.

Comment: From above eight examples, we can see that both the finite volume and finite difference HWENO schemes work well in comparison with their "exact" solutions. Further-

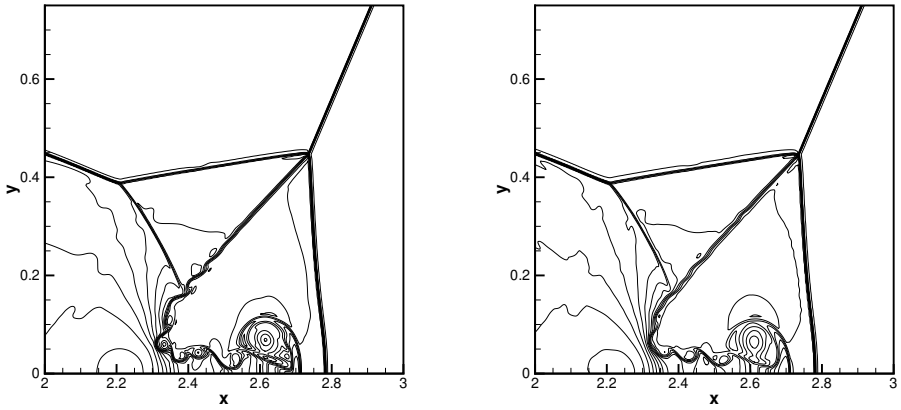

Figure 3.10: Double Mach reflection problem. $T = 0.2$. 30 equally spaced density contours from 1.5 to 22.7, zoom-in pictures around the Mach stem. Left: HWENO6-FV; right: HWENO4-FD. Number of cells: 1600×400 in the region of $[0, 4]\times[0, 1]$.

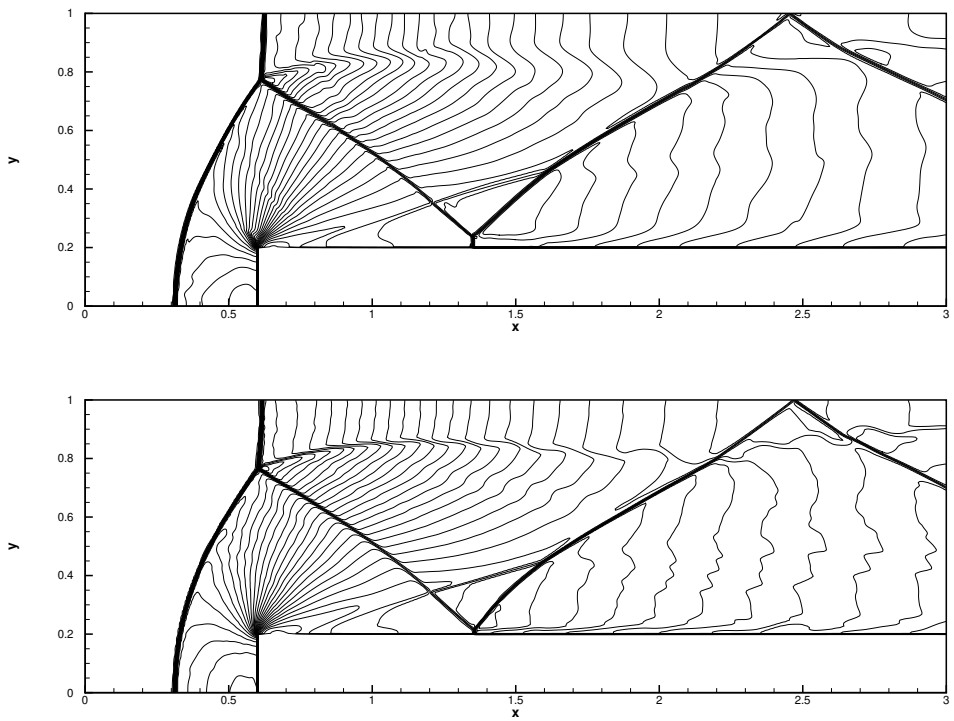

Figure 3.11: Forward step problem. $T = 4$. 30 equally spaced density contours from 0.32 to 6.15. Top: HWENO6-FV; bottom: HWENO4-FD. Number of cells: 600×200 in the region of $[0, 3]\times[0, 1]$.

more, there is not much difference between these two schemes for Example 3.6 and Example 3.7, while the finite volume HWENO schemes have better resolutions and sharper shock transitions than the finite difference HWENO schemes on the same meshes for the other examples except Example 3.10 and Example 3.13. This might be due to the fact that very global Lax-Friedrichs flux splitting (where α is chosen as a scalar for all components and all cells) is used in the finite difference scheme, causing larger numerical viscosity than the finite volume scheme. Also, for the two dimensional case, an extra obvious reason is that the finite volume HWENO scheme has a higher order of accuracy. We note that for Example 3.10 and Example 3.13, the result of the finite difference HWENO scheme is actually better than that of the finite volume scheme, the reason of this is not clear.

4 Concluding remarks

In this paper, we have designed a new type of finite volume and finite difference multi-resolution HWENO schemes for solving the hyperbolic conservation laws in one and two dimensional cases on structured meshes. In comparison with the classical HWENO schemes, the new features of these HWENO schemes are their simplicity since we only need to perform the spatial HWENO reconstruction for the function values but perform high-order linear reconstruction for its first-order derivative values and hierarchical structure in obtaining increasingly higher order of accuracy with unequal sized hierarchical central spatial stencils. These HWENO schemes are achieved by artificially setting positive linear weights as long as their sum equals one, calculating smoothness indicators, designing new nonlinear weights, and then obtaining a nonlinear convex combination of all the candidate polynomials. The features which are attractive include that there is no need to modify the first-order derivative values of the target cell before the reconstruction; no need to apply any positivity-preserving flux limiter for simulations with strong shocks, at least for the examples we have calculated in this paper; and that the CFL number can be taken to be 0.6 for both the one and two dimensional cases, which is an improvement from 0.2 in [15, 16]. In comparison with the

multi-resolution WENO schemes, our major advantage is the compactness in the reconstruction. The framework of this multi-resolution HWENO spatial reconstruction procedure would be particularly efficient and simple on unstructured meshes, the study of which is our ongoing work.

References

[1] D.S. Balsara, S. Garain, V. Florinski and W. Boscheri, An efficient class of WENO schemes with adaptive order for unstructured meshes, J. Comput. Phys., 404 (2020), 109062.

[2] D.S. Balsara, S. Garain and C.-W. Shu, An efficient class of WENO schemes with adaptive order, J. Comput. Phys., 326 (2016), 780-804.

[3] D.S. Balsara, C.-W. Shu, Monotonicity preserving weighted essentially non-oscillatory schemes with increasingly high order of accuracy, J. Comput. Phys., 160 (2000), 405-452.

[4] M. Castro, B. Costa, W.S. Don, High order weighted essentially non-oscillatory WENO-Z schemes for hyperbolic conservation laws, J. Comput. Phys., 230 (2011), 1766-1792.

[5] B. Cockburn, C.-W. Shu, TVB Runge-Kutta local projection discontinuous Galerkin finite element method for conservation laws II: general framework, Math. Comput., 52 (1989), 411-435.

[6] B. Costa and W.S. Don, Multi-domain hybrid spectral-WENO methods for hyperbolic conservation laws, J. Comput. Phys., 224 (2007), 970-991.

[7] M. Dumbser, W. Boscheri, M. Semplice and G. Russo, Central WENO schemes for hyperbolic conservation laws on fixed and moving unstructured meshes, SIAM J. Sci. Comput., 39 (2017), A2564-A2591.

[8] A. Harten, High resolution schemes for hyperbolic conservation laws, J. Comput. Phys., 49 (1983), 357-393.

[9] A. Harten, B. Engquist, S. Osher, S. Chakravarthy, Uniformly high order accurate essentially non-oscillatory schemes, III, J. Comput. Phys., 71 (1987), 231-303.

[10] C. Hu, C.-W. Shu, Weighted essentially non-oscillatory schemes on triangular meshes, J. Comput. Phys., 150 (1999), 97-127.

[11] G. Hu, R. Li, T. Tang, A robust WENO type finite volume solver for steady Euler equations on unstructured grids, Commun. Comput. Phys., 9 (2011), 627-648.

[12] G.-S. Jiang, C.-W. Shu, Efficient implementation of weighted ENO schemes, J. Comput. Phys., 126 (1996), 202-228.

[13] D. Levy, G. Puppo and G. Russo, Central WENO schemes for hyperbolic systems of conservation laws, Math. Model. Numer. Anal., 33 (1999), 547-571.

[14] D. Levy, G. Puppo, G. Russo, Compact central WENO schemes for multidimensional conservation laws, SIAM J. Sci. Comput., 22 (2000), 656-672.

[15] H. Liu, J. Qiu, Finite difference Hermite WENO schemes for conservation laws, J. Sci. Comput., 63 (2015), 548-572.

[16] H. Liu, J. Qiu, Finite difference Hermite WENO schemes for conservation laws, II: an alternative approach, J. Sci. Comput., 66 (2016), 598-624.

[17] X.D. Liu, S. Osher, T. Chan, Weighted essentially non-oscillatory schemes, J. Comput. Phys., 115 (1994), 200-212.

[18] S. Pirozzoli, Conservative hybrid compact-WENO schemes for shock-turbulence interaction, J. Comput. Phys., 178 (2002), 81-117.

[19] J. Qiu, C.-W. Shu, Hermite WENO schemes and their application as limiters for Runge-Kutta discontinuous Galerkin method: one-dimensional case, J. Comput. Phys., 193 (2004), 115-135.

[20] J. Qiu, C.-W. Shu, Hermite WENO schemes and their application as limiters for Runge-Kutta discontinuous Galerkin method II: two-dimensional case, Computers and Fluids, 34 (2005), 642-663.

[21] C.-W. Shu, Essentially non-oscillatory and weighted essentially non-oscillatory schemes for hyperbolic conservation laws, in Advanced Numerical Approximation of Nonlinear Hyperbolic Equations, B. Cockburn, C. Johnson, C.-W. Shu and E. Tadmor (Editor: A. Quarteroni), Lecture Notes in Mathematics, volume 1697, Springer, Berlin, 1998, pp.325-432.

[22] C.-W. Shu, S. Osher, Efficient implementation of essentially non-oscillatory shock capturing schemes, J. Comput. Phys., 77 (1988), 439-471.

[23] C.-W. Shu, S. Osher, Efficient implementation of essentially non-oscillatory shock capturing schemes, II, J. Comput. Phys., 83 (1989), 32-78.

[24] Z.J. Wang, R.F. Chen, Optimized weighted essentially non-oscillatory schemes for linear waves with discontinuity, J. Comput. Phys., 174 (2001), 381-404.

[25] Y.H. Zahran and A.H. Abdalla, Seventh order Hermite WENO scheme for hyperbolic conservation laws, Comput. Fluid., 131 (2016), 66-80.

[26] Z. Zhao, Y. Chen, J. Qiu, A hybrid Hermite WENO scheme for hyperbolic conservation laws, J. Comput. Phys., 405 (2020), 109175.

[27] Z. Zhao, J. Qiu, A Hermite WENO scheme with artificial linear weights for hyperbolic conservation laws, J. Comput. Phys., 417 (2020), 109583.

[28] J. Zhu, J. Qiu, A class of fourth order finite volume Hermite weighted essentially non-oscillatory schemes, Sci. China Ser. A, Math., 51 (2008), 1549-1560.

[29] J. Zhu, C.-W. Shu, A new type of multi-resolution WENO schemes with increasingly higher order of accuracy, J. Comput. Phys., 375 (2018), 659-683.

[30] J. Zhu, C.-W. Shu, A new type of multi-resolution WENO schemes with increasingly higher order of accuracy on triangular meshes, J. Comput. Phys., 392 (2019), 19-33.